Preliminary Design of a Solar-Powered Hybrid Airship

Howard P. Buckley [*] , Nick Holt [†] , Andrew Leinonen [‡]

Sebastien Fournier [§] , and David W. Zingg [¶]

Institute for Aerospace Studies, University of Toronto

4925 Dufferin St., Toronto, Ontario, M3H 5T6, Canada

The feasibility of a solar-powered hybrid airship where lift is generated by both buoyancy and aerodynamics is investigated using aerodynamic shape optimization. The design objective is to minimize the product of envelope root chord and span (which corresponds to the size of hangar required to house the airship), subject to constraints on lift, ratio of solar power produced to power consumed, airship operational empty weight, trim, and static margin. Simple mass models are used to estimate the mass of airship components, including the solar array, drive train components, and envelope fabric. The optimizer has the freedom to vary the envelopes section shapes, span, twist, angle of attack, and flap angle. A three-point optimization has produced a feasible envelope geometry that satisfies the design requirements at two 46 km/h cruise speed operating conditions, each with a centre-of-gravity location at either extreme of the design range, and one low-speed operating condition. The results indicate that such an aircraft, which could be well suited to operations in remote areas, is feasible with respect to aerodynamic efficiency. Sensitivity studies indicate that faster hybrid airships will become feasible with future improvements in solar panel irradiance.

[*]Senior Research Associate, howard@oddjob.utias.utoronto.ca

[†]Aerospace EIT, Solar Ship Inc. nholt@solarship.com

[‡]Lead Industrial Designer, Solar Ship Inc. aleinonen@solarship.com

[§]Chief Innovation Officer, Solar Ship Inc. sfournier@solarship.com

[¶]Professor, University of Toronto Distinguished Professor of Computational Aerodynamics and Sustainable Aviation, dwz@oddjob.utias.utoronto.ca

Nomenclature

β Side-slip angle

ϵ Landing gear mass scaling factor

η_{motor} Motor efficiency

η_{prop} Propeller efficiency

γ Control surface actuator power consumption rate

Γ_x Distance in the streamwise direction between the envelope volume centroid and the centre of gravity

Γ_y Distance in the spanwise direction between the envelope volume centroid and the centre of gravity

Γ_z Distance in the vertical direction between the envelope volume centroid and the centre of gravity

κ_1 Envelope fabric mass constant 1

κ_2 Envelope fabric mass constant 2

κ_3 Envelope fabric mass constant 3

κ_4 Ballonet fabric mass constant

λ Fuselage drag constant

Ω Fuselage reinforcement factor

Φ Solar panel density

Π Payload reinforcement factor

ρ_{air} Air density

ρ_{batt} Battery energy density

ρ_{CS} Control surface density

ρ_{motor} Motor power density

σ_{max} Maximum tensile fabric stress

Ξ Ballonet fan power consumption rate

A Envelope surface area

A_{CS} Control surface area

C_D Coefficient of drag (CFD)

C_L Coefficient of lift

C_l Coefficient of roll moment

C_m Coefficient of pitch moment

C_n Coefficient of yaw moment

C_Y Coefficient of side force

C_{D_X} Coefficient of drag (excrescence)

C_{L_α} Sensitivity of lift to angle of attack

C_{M_α} Sensitivity of pitching moment to angle of attack

D_{CFD} Drag (CFD)

D_{G} Drag (fuselage)

D_{Total} Drag (total)

D_{X} Drag (excrescence)

g Acceleration due to gravity

H Solar array area coverage

h Average envelope height

I Solar array irradiance

K_n Static margin

L_{aero} Lift (aerodynamic)

L_{buoy} Lift (buoyant)

M_{aero} Pitching moment (aerodynamic)

M_{buoy} Pitching moment (buoyant)

m_{airship} Airship mass

m_{ballFab} Ballonet fabric mass

m_{ballGas} Ballonet gas mass

m_{battRsrv} Reserve battery mass

m_{ctrlSurf} Control surface mass

$m_{\text{envFab-Ext}}$ Envelope fabric mass (exterior)

$m_{\text{envFab-Int}}$ Envelope fabric mass (interior)

m_{envFab} Envelope fabric mass

m_{envGas} Envelope gas mass

m_{env} Envelope mass

m_{fuse} Fuselage mass

m_{motor} Motor mass

m_{payload} Payload mass

m_{pilot} Pilot mass

$m_{\text{solarArray}}$ Solar array mass

M_{total} Pitching moment (total)

q Dynamic pressure

S Envelope projected area

V Envelope volume

v Airship velocity

V_{ballonet} Ballonet volume

V_{buoy} Buoyant volume

W_{airship} Airship weight

CG Centre of gravity

MAC Mean aerodynamic chord

RC Root Chord

I. Introduction

The term *hybrid airship* is used to characterize aircraft where lift is generated from both buoyancy and aerodynamics. In addition to producing buoyant and aerodynamic lift, the inflatable wing, referred to as the envelope, also provides a substantial surface upon which to mount a solar array for the vehicle's sole source of power. The objective of the present work is to develop a preliminary aerodynamic design of the envelope of a solar-powered hybrid airship through the application

of aerodynamic shape optimization based on the Reynolds-averaged Navier-Stokes (RANS) equations.

The intended mission for the proposed hybrid airship is to provide disaster relief to remote areas of central Africa, where roads may be non-existent or impassable for various reasons. Its primary purpose is as a mode of transportation for light payloads that does not depend on fossil fuel, roads, or runways. Solar power is a natural choice for such a vehicle due to the scarcity of fossil fuel and associated high operating costs combined with a year-round abundance of high-intensity sunshine in the region. A payload capacity of 500 kg is sufficient to transport essentials such as food and medical supplies. A fleet of solar-powered hybrid airships stationed at a regional hub where supplies are readily available may be deployed to remote areas within a 370 km radius. This range is the distance that can be traversed at a cruise speed of 46.3 km/h during eight hours of daylight. These remote areas are often inaccessible by land transportation due to poor road infrastructure and unfavourable weather conditions. In some locations, a soccer field may be the closest thing to a runway, so the airship must be capable of landing and taking off in a short distance of 100 meters or less. After the cargo is unloaded at the destination, the vehicle must still be heavy enough to exceed the buoyant lift force by at least 10% to keep it grounded. The envelope's maximum wing span of 48 metres and maximum height of 13 metres are dictated by the door dimensions of an existing hangar through which it must pass.

In a typical aerodynamic shape optimization, an objective function is minimized such that fuel-burn is minimized for a given range, or range is maximized for a given amount of fuel. For a fully solar-powered vehicle the concepts of fuel-burn and range do not apply. In the present application, the challenge faced by the designer is to keep the vehicle from becoming too large, which is disadvantageous in several respects. Hence we minimize the required hangar area in order to design the smallest possible vehicle that meets the operating requirements associated with power, field length, anchor factor, and stability. The design cruise speed is 46.3 km/h in order to enable operation in the presence of a modest headwind. Table 1 summarizes the high-level design requirements.

There are several examples found in the literature of aerodynamic shape optimization applied to

airship and hybrid airship design using low-fidelity analysis methods. An early example of shape optimization by Lutz and Wagner [1] was applied to an axisymmetric airship, and shapes were optimized for minimum drag for a given envelope volume in different Reynolds number regimes. This investigation made use of a potential flow method coupled with a boundary layer code and a transition prediction method. Haque et al. [2] developed a concept for a two-seat winged hybrid airship designed to carry 1000 kg. In a follow up paper, Haque et al. proposed a hybrid airship to connect the Malaysian Islands and suggests examining the benefits of replacing an existing fleet of STOL aircraft with hybrid buoyant aircraft with similar capabilities [3]. A concept design for a winged hybrid airship was presented by Hartmann [4] which features a lifting body hull to augment lift. Hartmann recognized that there were nonlinearities in the aerodynamics of the unconventional envelope shape and developed a surrogate model from a database of CFD results to capture these nonlinearities and their effects on stability and performance. A high altitude fully solar hybrid airship concept was developed by Zhang et al. [5]. The concept was a three-lobe configuration and a genetic optimization algorithm was free to adjust planform area, buoyancy ratio, and airspeed while meeting lift constraints and minimizing total aircraft weight. Several optimizations were performed for different seasonal and geographic locations. It was found that buoyancy ratios between 60% and 70% were ideal for this concept through the year except during winter where higher buoyancy ratios were needed. The concepts designed for winter flight were geographically restricted in feasible latitudes due to reduced solar irradiance.

The next section describes the aerodynamic shape optimization methodology used. This is followed by a description of the grid used for the numerical solution of the RANS equations and the geometry control system used to enable the optimization algorithm to modify the envelope geometry. Next the optimization problem formulation is presented in detail. Finally, the results are presented and discussed, comprising sensitivity studies to critical design parameters, the 3-point optimized envelope design, and fine-mesh analysis of the optimized envelope.

Payload	500 kg
Crew	1 pilot at 84 kg
Range	370 km
Cruise	46.3 km/h at 3500 m
Power	solar array to provide 100% of power required for propulsion and auxiliary systems
Takeoff and Landing	field length of 100 m, 25 km/h all types of runway surfaces
Hangar Size	airship must pass through hangar door (48 m width x 13 m height)
Anchor Factor	airship OEW must be at least 10% greater than buoyant lift at sea level
Pitching Static Margin	$\geq$ 5% MAC
CG Range	0.345 - 0.395 (location along the longitudinal axis as a fraction of root-chord length)
Trim	airship must be trimmable over the range of CG locations

Table 1. Design Requirements

II. Jetstream Aerodynamic Shape Optimization Methodology

Jetstream is an aerodynamic shape optimization methodology [6, 7] that has been used in several studies of unconventional aircraft configurations [8–11]. It has been demonstrated to be a state-of-the-art methodology through application to the suite of test problems defined by the Aerodynamic Design Optimization Discussion Group of the American Institute of Aeronautics and Astronautics and several other problems that confirm its ability to solve challenging optimization problems involving substantial geometric changes [12, 13]. The algorithm consists of a three-dimensional flow solver for the RANS equations [14], a free-form and axial deformation geometry control approach controlling a B-spline geometry parameterization which is coupled with an integrated linear elasticity mesh deformation strategy [6], and the gradient-based optimizer SNOPT [15] with gradients calculated using the discrete adjoint method. [16]

The flow solver is used to evaluate the aerodynamic properties of the geometry at each design iteration during an optimization. It solves the compressible RANS equations with the Spalart-Allmaras turbulence model using a parallel Newton-Krylov-Schur method. Given the Reynolds number for the current application (18.5 million) and the expected manufacturing approach, fully-turbulent flow is assumed. The linear system arising at each Newton iteration is solved using the

flexible generalized minimal residual method (FGMRES) preconditioned with an approximate-Schur preconditioner. The solver is based on multi-block structured grids and utilizes summation-by-parts finite-difference operators to discretize spatial derivatives, and simultaneous approximation terms to handle block interfaces and boundary conditions. The flow solver has been thoroughly verified through test cases from the NASA Langley Research Center Turbulence Modeling Resource (https://turbmodels.larc.nasa.gov) and validated through participation in the 5th Drag Prediction Workshop [17].

Deformation of the aerodynamic geometry is handled by a two-level free-form and axial deformation approach [10]. Axial curves handle variations in sweep, span, and dihedral, while free-form-deformation (FFD) volumes handle variations in twist, taper, and section shape. Both the axial curves and the FFD volumes are modelled with B-splines whose control points are used as design variables in the optimization. At each design iteration, the grid surrounding the modified geometry is perturbed using a linear elasticity grid deformation technique applied to the control points of B-spline volumes that are fitted to each block of the computational grid. Gradients of the design problem objective and constraints are calculated using the discrete adjoint method. Given the objective, constraints, and their respective gradients, the design variable update at each design iteration is computed by SNOPT (Sparse Nonlinear OPTimizer), a general purpose algorithm for large scale constrained optimization problems developed by Gill et al [15]. Although this gradient-based approach is efficient, it finds a local minimum, as opposed to the global minimum in a non-convex problem. In the present study, the presence of multimodality has not been explored [18], so it is possible that an optimum exists within the design space with a lower objective function value, but based on experience it is unlikely to be significantly lower.

III. CFD Grid and Geometry Control System

Figure 1 shows a full-span envelope that is the basis for the initial envelope geometry used in all optimization cases performed for this work. It has a wing span of 48 meters, a root-chord length of 46 meters, and a maximum thickness of 13 meters. As optimization on a fine mesh is too computationally intensive at the present time, the current best practice in aerodynamic shape optimization

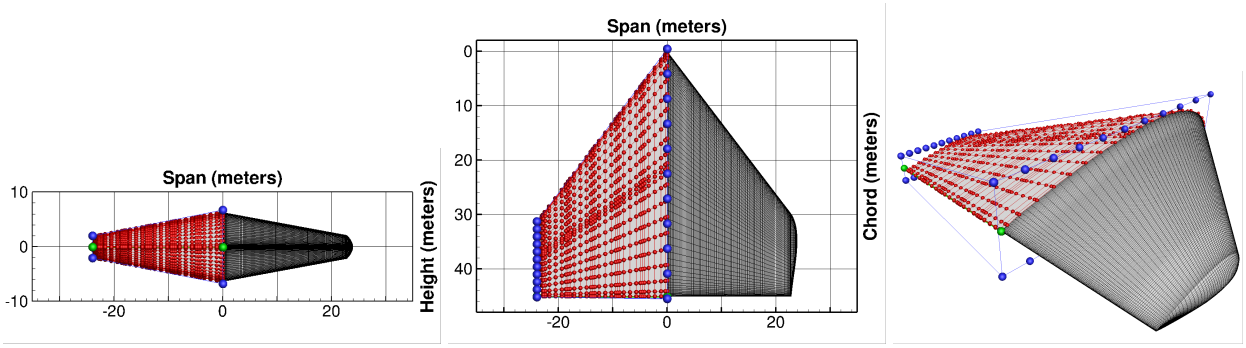

a) yz view b) xy view c) iso view

Figure 1. Envelope geometry for optimization cases showing CFD grid (black), FFD volume control points (blue), axial curve control points (green), envelope surface control points (red) embedded within FFD volume

is to conduct the optimization on a relatively coarse mesh followed by a fine-mash analysis of the optimized geometry [8]; this is the approach taken here. Since the optimization problem assumes a velocity vector with no side-slip component, a computational grid for a half-span envelope geometry is used to reduce the cost of flow simulations. At each design iteration of an optimization, aerodynamic performance of the half-span envelope is evaluated using a CFD grid with 2.3 million nodes partitioned over 64 blocks. Average y+ values for this grid are less than 0.5, indicating that the boundary layer is sufficiently resolved for accurate turbulence modelling. Based on results from a grid convergence study, the above grid can be expected to produce numerical errors in C_L and C_D of -7% and +8% respectively. To account for the over-prediction of C_D associated with the optimization grid described above, a correction factor of 0.95 is applied so that the performance of the envelope is not unduly penalized by power calculations that are a function of C_D. Furthermore, the final optimized geometry is re-evaluated using a full-span fine grid to confirm that performance objectives and design constraints are satisfied. The full-span optimized geometry is also evaluated over a small range of side-slip angles to analyze its performance when operating in a crosswind. Additional details of the grid convergence study, the drag correction factor, and the post-optimization fine-grid performance evaluation are presented in Section V-C.

The grid, including nodes on the envelope surface and in the surrounding fluid, is controlled by hexahedral B-spline volumes. The red spheres shown in Figure 1 are the control points of the B-spline volumes whose faces are coincident with the envelope surface. Deformation of the hybrid

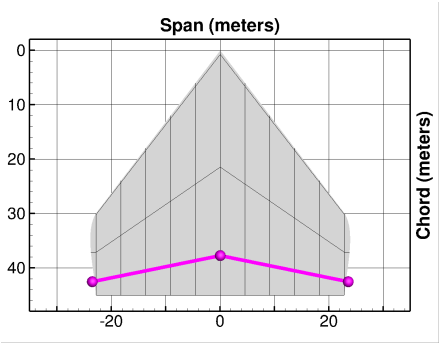

Figure 2. Initial envelope geometry showing location of trailing-edge flap hinge line (pink) at approximately 85% chord

airship envelope geometry at each design iteration of the optimization is handled by a geometry control system based on two-level free-form and axial deformation. The optimizer can move the B-spline control points that define the free-form deformation (FFD) volume (blue spheres) and the axial curve (green spheres). The red envelope control points embedded within the FFD volume modify the envelope geometry corresponding to coordinated movements of the FFD volume and axial curve. Using this technique, the axial curve handles variations in sweep, span, and dihedral, while the FFD volume handles variations in twist, taper, and section shape.

In all optimization cases presented, the axial curve represented by two control points is linear and coincident with the trailing-edge of the envelope. The axial control point at the envelope root is fixed, while the axial control point at the tip is permitted to move only in the spanwise direction, i.e. sweep and dihedral are fixed. The FFD volume has two sections, one at the root and one at the tip. Each FFD section has 22 control points split evenly between upper and lower surfaces. The optimizer can vary chord length and section shape at both the root and tip, while only the tip section is allowed to twist (about the axial curve). Envelope sections in between the root and tip are linearly interpolated.

To trim the hybrid airship, a trailing-edge flap is simulated by a coordinated movement of FFD section control points that are aft of 85% of the length of the respective section. Figure 2 shows the position of the flap hinge line. The angle of attack and flap angle are chosen such that the lift generated by both aerodynamic forces and buoyancy equals the weight and the pitching moment about the center of gravity is zero.

IV. Optimization Problem Description

The optimization problem can be summarized as follows.

minimize	(Span) x (Root Chord)
w.r.t.	Envelope sectional shape variables
	Envelope planform variables
	Envelope twist variables
	Angle of attack
	Flap angle
subject to	$L_{\text{aero}} + L_{\text{buoy}}$ = Total Airship Weight (lift constraint)
	Power Factor ≥ 1
	Airship OEW $\geq 1.1 L_{\text{buoy}}$ (anchor constraint)
	$\left(M_{\text{aero}} + M_{\text{buoy}}\right)^{\text{CG}}_{\text{pitching}} = 0$ (trim constraint)
	$K_n \geq 5\%$ MAC (static margin constraint)
	Envelope taper ≥ 1.0
	Fixed sweep and dihedral angles
	Near-linear leading- and trailing-edges

The preliminary envelope design for the solar-powered hybrid airship is achieved by performing a 3-point optimization with a design objective to minimize the product of envelope span and root chord. This design objective is chosen to achieve the practical goal of minimizing the foot print of a hangar constructed to house the hybrid airship. The multi-point optimization is motivated by the requirement to have the hybrid airship capable of operating at cruise conditions over a range of expected CG locations, and also of operating at a low-speed condition at sea level, such that the hybrid airship is statically stable during landing and take-off. The two cruise operating conditions have a velocity of 46.3 km/h and an altitude of 3500 meters. They are identical with

the exception of CG location; for each operating condition, the longitudinal coordinate of the CG location is constrained to be at 34.5% and 39.5% of the root chord length measured from the nose of the hybrid airship, respectively. These CG locations represent the extreme forward and aft limits of the CG range. The additional low-speed operating condition has a velocity of 35 km/h and is at sea level.

The Power Factor is the ratio of power produced from the solar array to the total power consumption of the hybrid airship:

$$\text{Power Factor} = \text{Solar Power Produced/Total Power Consumed} \tag{1}$$

Solar Power Produced is defined as:

$$\text{Solar Power Produced} = S \times H \times I \tag{2}$$

where S is the envelope projected area, H is solar array area coverage, and I is the maximum solar array irradiance. Values used for H and I are given in Table 2. Total Power Consumed by the hybrid airship is the sum of power consumed by the propulsion system and the power consumed by auxiliary systems:

$$\text{Total Power Consumed} = \text{Propulsion Power} + \text{Auxiliary Power} \tag{3}$$

$$\text{Propulsion Power} = vD_{\text{Total}}\left(\frac{1}{\eta_{prop}}\right)\left(\frac{1}{\eta_{motor}}\right) \tag{4}$$

$$\text{Auxiliary Power} = \Xi V + \gamma A_{CS} \tag{5}$$

where v is the hybrid airship velocity, η_{prop} and η_{motor} are efficiencies of propellers and electric motors, Ξ and γ are rates of power consumption associated with ballonet fans and control surface actuators, V is the envelope volume, A_{CS} is the surface area of the control surfaces, and D_{Total} is

the total hybrid airship drag given by

$$D_{\text{Total}} = D_{\text{CFD}} + D_{\text{G}} + D_{\text{X}} \tag{6}$$

D_{CFD} is the drag produced by the envelope geometry computed using the flow solver. Based on the results of a grid convergence study, a correction factor of 0.95 is applied to D_{CFD} to account for the flow solver's over-prediction of the computed drag coefficient on the grid used in the optimization. D_{G} is the estimated drag produced by the fuselage geometry, and D_{X} is the estimated drag associated with envelope features not included in the envelope geometry such as envelope lobes and gaps between envelope and control surfaces. Expressions for D_{CFD}, D_{G} and D_{X} are given by

$$D_{\text{CFD}}(v) = \frac{1}{2}\rho_{\text{air}} v^2 \left[0.95 C_D\right] S \tag{7}$$

$$D_{\text{G}}(v) = \lambda v^2 \tag{8}$$

$$D_{\text{X}}(v) = \frac{1}{2}\rho_{\text{air}} v^2 \left[C_{D_X}\right] S \tag{9}$$

where λ is a constant, and C_D and C_{D_X} are the coefficients of computed drag and envelope excrescence drag.

Total lift generated by the envelope is the sum of contributions from aerodynamic and buoyant lift. Aerodynamic lift is calculated using the lift coefficient C_L computed by the flow solver. The volume used in the buoyancy calculation is the total volume of the envelope geometry that represents the combined volume of the envelope and elevon control surfaces. Buoyant Lift is equal to the weight of the volume of air displaced by the envelope geometry used in the optimization:

$$L_{\text{buoy}} = \rho_{\text{air}} V_{\text{buoy}} g \tag{10}$$

where ρ_{air} is the density of air at cruise altitude, and g is the acceleration due to gravity. The total hybrid airship weight is given by

$$W_{\text{airship}} = m_{\text{airship}} g \tag{11}$$

$$m_{\text{airship}} = \epsilon(m_{\text{env}} + m_{\text{fuse}} + m_{\text{ctrlSurf}} + m_{\text{payload}} + m_{\text{pilot}}) \tag{12}$$

where ϵ is a mass scaling factor for the landing gear. Envelope mass is given by

$$m_{\text{env}} = m_{\text{envFab}} + m_{\text{envGas}} + m_{\text{ballFab}} + m_{\text{ballGas}} + m_{\text{solarArray}} \tag{13}$$

where m_{envFab}, m_{ballFab}, m_{envGas}, and m_{ballGas} are the masses of the envelope and ballonet fabrics and gases. Helium is used to inflate the envelope volume, although this will likely not be the preferred gas in practice due to its limited availability. The ballonet is an inflatable air-filled bag enclosed within the envelope used to regulate internal pressure, density, and buoyant lift with changes in altitude. Its volume varies from 30% of the total volume enclosed by the envelope at sea level to 0% at the design cruise altitude of 3500 meters. The masses of helium and air are calculated using their respective densities and volumes. Envelope fabric mass is the sum of fabric masses for the envelope's external shell and its internal webbing:

$$m_{\text{envFab}} = m_{\text{envFab-Ext}} + m_{\text{envFab-Int}} \tag{14}$$

$$m_{\text{envFab-Ext}} = \kappa_1 \sigma_{\max} A \tag{15}$$

$$m_{\text{envFab-Int}} = \kappa_3 \sigma_{\max} V \tag{16}$$

At each design iteration, a simple model representing the maximum fabric tensile stress is used to estimate the fabric strength required to support the envelope loading from bending moments and from the envelope's internal pressure. To prevent buckling during flight, the top and bottom surfaces of the envelope must always be in tension. This is accomplished by inflating the envelope to an internal pressure that produces a tensile stress in the fabric that exceeds the magnitude of the stress due to bending moments. In the above envelope fabric mass equations, κ_1, κ_2, and κ_3 are constants, A is the envelope surface area, and $\sigma_{\max}$ is a representation of the maximum tensile fabric stress given by the following equation:

$$\sigma_{\max} = (\kappa_2 + 1)\left(\frac{M_{\text{Total}}}{h^2}\right) \tag{17}$$

The moment M_{Total} is the sum of aerodynamic and buoyant root bending moments, and h is the average height of the envelope. The quantity $\frac{M_{\text{Total}}}{h^2}$ serves as a proxy for the fabric stress due to M_{Total}. The maximum tensile fabric stress occurs on the bottom surface of the envelope and is equal to the sum of the stresses due to M_{Total} and internal pressure. On the top surface of the envelope the stress due to M_{Total} is compressive and hence is subtracted from the stress due to internal pressure. A value for κ_2 that is greater than one indicates that the fabric is strong enough to withstand a bottom-surface stress that is more than double the stress due to M_{Total}. This condition occurs when fabric stress due to internal pressure is greater than that due to M_{Total}. Ballonet fabric mass is calculated using an estimate of its surface area (based on its volume at sea level) given by

$$m_{\text{ballFab}} = \kappa_4 V_{\text{ballonet}}^{\frac{2}{3}} \tag{18}$$

where κ_4 is a constant, and V_{ballonet} is the ballonet volume at sea level.

Solar array mass varies with envelope surface area and is calculated as follows:

$$m_{\text{solarArray}} = AH\Phi \tag{19}$$

where Φ is solar panel density.

Fuselage mass is given by

$$m_{\text{fuse}} = \Psi + \Omega\,(m_{\text{motor}} + m_{\text{battRsrv}}) \tag{20}$$

where Ψ is a constant representing a base mass for the fuselage, and Ω is a fuselage reinforcement factor. The masses of components in the propulsion system are scaled in proportion to their associated power requirements:

$$m_{\text{motor}} = (\text{Power Motor})\rho_{\text{motor}} \tag{21}$$

$$m_{\text{battRsrv}} = (\text{Auxiliary Power})(\text{battRsrvTime})\rho_{\text{batt}} \tag{22}$$

where ρ_{motor}, and ρ_{batt} are power densities to represent component mass per unit of power. The mass of control surfaces is given by

$$m_{\text{ctrlSurf}} = (A_{CS})(\rho_{\text{CS}}) \tag{23}$$

where ρ_{CS} is a control surface density representing control surface mass per unit of control surface surface area. Payload mass is given by

$$m_{\text{payload}} = \Pi(\text{Payload Mass}) \tag{24}$$

where Π is a payload reinforcement factor. Pilot mass m_{pilot} is a constant defined as an input parameter. Assuming a small angle of attack, buoyant pitching moment is approximated as

$$M_{\text{buoy}} = L_{\text{buoy}}\Gamma_x \tag{25}$$

where Γ_x is the distance in the streamwise direction between the envelope volume centroid and the centre of gravity. The static margin with contributions from both aerodynamic, and buoyant pitching moments is given by

$$K_n = -\frac{C_{M_\alpha}}{C_{L_\alpha}} - \frac{L_{\text{buoy}}\Gamma_z}{qS\,C_{L_\alpha}\text{MAC}} \tag{26}$$

where C_{M_α} and C_{L_α} are calculated using forward-biased finite differences, Γ_z is the vertical distance between the envelope volume centroid and the centre of gravity, and q is the dynamic pressure.

Practical considerations regarding the current state of solar panel technology and the requirements of disaster relief missions provided the basis for selecting the values of solar panel efficiency (maximum irradiance), I, solar panel density, Φ, and payload. A summary of the parameters used in the optimization case presented in this work is given in Table 2.

Motor Power Density, ρ_{motor}	0.588	$\frac{kg}{kW}$
Battery Energy Density, ρ_{batt}	9.000	$\frac{kg}{kWh}$
Control Surface Density, ρ_{CS}	3.846	$\frac{kg}{m^2}$
Motor Efficiency, η_{motor}	0.95	-
Propeller Efficiency, η_{prop}	0.75	-
Ballonet Fraction (At Altitude)	0.0	-
Ballonet Fraction (At Sea Level)	0.295	-
Air Density (At Altitude), ρ_{air}	0.8630	$\frac{kg}{m^3}$
Air Density (At Sea Level), $\rho_{\text{air-SL}}$	1.225	$\frac{kg}{m^3}$
Envelope Gas Density (At Altitude), ρ_{envGas} (He)	0.1640	$\frac{kg}{m^3}$
Area Coverage, H	0.70	-
Max Irradiance, I	130	$\frac{W}{m^2}$
Fuselage Drag Factor, λ	3.246	$\frac{kgs^4}{m^3}$
C_{D_X} (envelope excrescence drag)	0.010	-
Payload Weight	500	kg
Solar Panel Density, Φ	0.72	$\frac{kg}{m^2}$
κ_1	1.10×10^{-5}	-
κ_2	3.5	-
κ_3	2.69×10^{-6}	-
κ_4	1.16	-
Velocity, v	12.86	$\frac{m}{s}$
Altitude	3500	m
Reynolds Number	18.5×10^6	-
Ballonet Power Consumption, Ξ	0.0028	$\frac{kW}{m^3}$
CS Actuator Power Consumption, γ	0.1231	$\frac{kW}{m^2}$
Range	370	km
Battery Reserve Time	0.4	h
Fuselage Basic Mass, Ψ	800	kg
Pilot Mass	84	kg
Fuselage Reinforcement Factor, Ω	1.05	-
Payload Reinforcement Factor, Π	1.05	-
Landing Gear Mass Factor, ϵ	1.05	-

Table 2. Design parameters for the hybrid airship mission

V. Results

A. Sensitivity Studies

To determine the sensitivity of the envelope design to critical design parameters, a suite of studies was performed. Each study focused on a parameter of interest wherein optimization cases were performed over a range of values for the parameter. Figure 3 shows plots of the hangar area design objective (Root Chord x Span) versus parameter values for solar panel irrandiance I, cruise speed v, fuselage (gondola) drag factor λ, coefficient of excrescence drag C_{D_X}, altitude, and CG location. The plots indicate that hangar area is significantly impacted by changes to solar panel irradiance, cruise speed, and fuselage drag factor. A slight sensitivity is shown to excrescence drag, and

negligible sensitivity to altitude and CG location.

The total power consumption requirements of the vehicle must be satisfied by the solar panel array mounted to the top surface of the envelope. With greater solar panel irradiance I, the array can produce the required power with a smaller envelope projected area S. Reduction in envelope projected area also helps to reduce envelope drag, which reduces power requirements for propulsion. Changes to cruise speed are bound to impact the hangar area objective since propulsion power is proportional to its cube. Table 8 shows that fuselage drag accounts for greater than one third of total drag at cruise speed. Therefore it is not surprising that changes to the fuselage drag factor λ will produce large swings in total drag and propulsive power requirements, with corresponding changes to the size of solar array and hence changes to the hangar area design objective.

The values for solar panel irradiance and fuselage drag factor are intentionally chosen to be conservative. The fuselage drag factor is based on a combination of flight data and CFD. Given the sensitivity to this parameter, further effort to refine this estimate is recommended. The solar panel irradiance is based on currently accepted values for the power available from the sunshine specific to the region (central Africa), a manufacturer's published values, and a conservative estimate of the efficiency of the vehicle's electrical system. It is apparent from the sensitivity studies that substantially smaller or faster vehicles will become possible as future technological advancements in solar panel efficiency are made.

B. Optimized Envelope Design

An optimal envelope design has been achieved that minimizes the hangar area design objective while maintaining feasibility with respect to all constraints based on the 3-point optimization problem formulation presented in Section IV. Its solution satisfies the Karush-Kuhn-Tucker [19] optimality conditions for a constrained optimization problem to within a tolerance of 1×10^{-6}. The optimized envelope geometry and pressure distributions for the lower-than-cruise-speed operating condition with CG at 37.5% x/RC (cg375) is shown in Figures 4 and 5[a]. Figures 6 - 9 display the results for the cruise operating conditions where CG is in the extreme-forward and -aft locations

[a]The small discontinuities seen at mid-chord in the pressure distributions of Figures 5, 7, and 9 are due to the flow solver's treatment of simultaneous approximation terms.

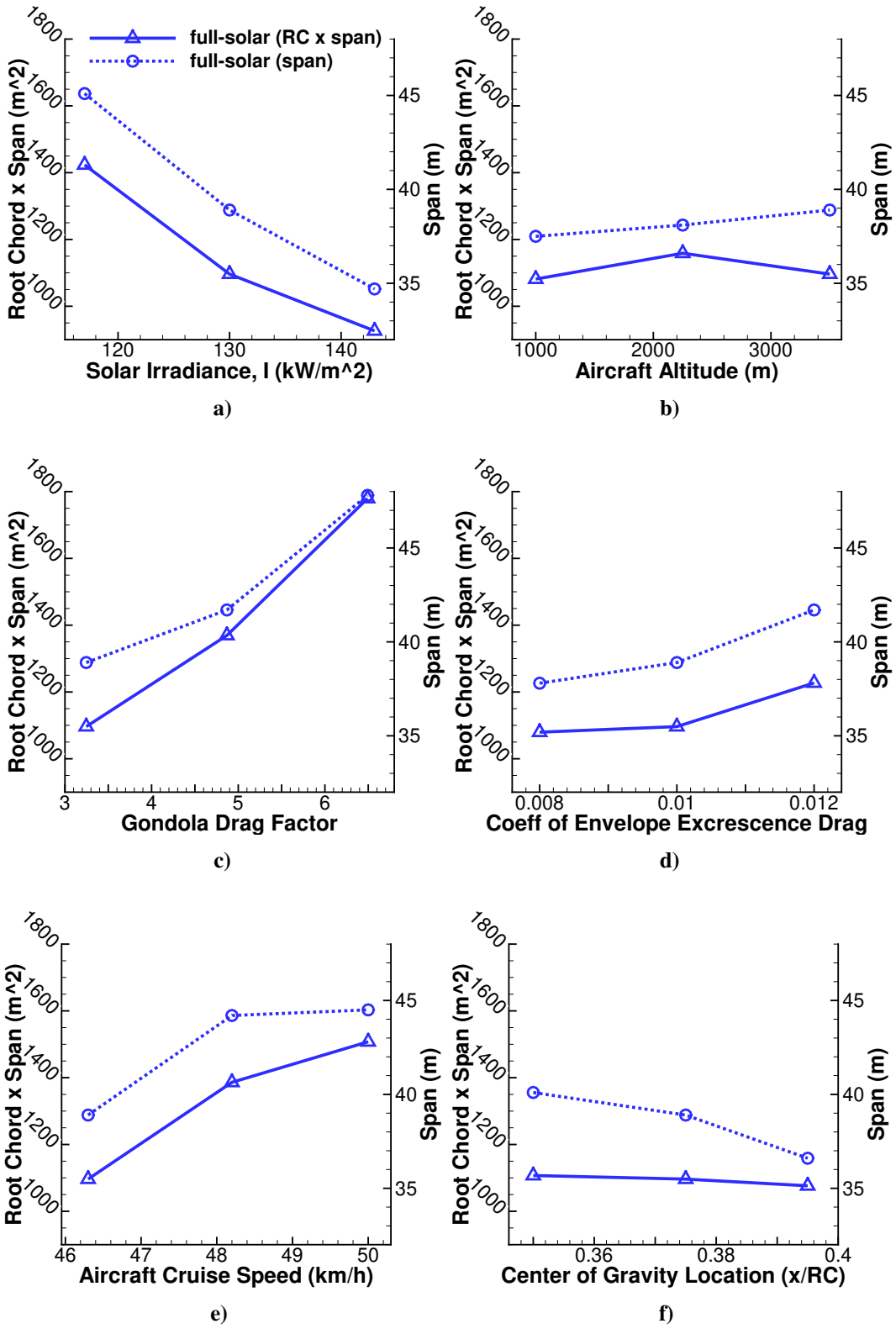

Figure 3. Sensitivity of hangar-area objective function to changes in various design parameters

geometry	Vel (kph)	Airship Mass (kg)	Airship Lift (kg)	AoA	Flap Angle	Eff Sol Array Area (m^2)	Solar Power (kW)	Total Pwr Cnsmd (kW)	Pwr Fac	Anc Fac	Hangar Area (m^2)
cg375	35.0	5148.3	5148.2	16.0°	−28.1°	570.3	74.1	55.7	1.33	1.10	1146.3
cg345	46.3	3980.5	3981.1	11.2°	−18.4°	574.0	74.6	74.6	1.00	1.10	1146.3
cg395	46.3	3973.3	3973.5	7.9°	0.4°	572.9	74.5	74.5	1.00	1.10	1146.3

Table 3. Performance summary, 3-point-optimized full-solar hybrid airship

(cg345, cg395). Tables 3-11 show the hybrid airship performance for the three operating conditions described above. As shown in Table 3, the hangar area for the optimal envelope design is 1146 m^2. With a span of 40.6 m, and a maximum envelope height of 9.0 m, listed in Table 4, the hybrid airship satisfies the geometric constraints imposed by the maximum allowable hangar door dimensions of 48 m width and 13 m height.

The only differences between the envelope geometries at each operating condition are the flap deflection angles and the angle of attack. The flap allows the hybrid airship to be trimmed at different altitudes, speeds, and CG locations. The low-speed operating condition (cg375) with CG at the mid-point of its range has the largest negative flap deflection (−28.1°). The cruise operating conditions (cg345 and cg395) have flap deflections of −18.4° and +0.41°, respectively. For the cruise operating conditions, when the CG is in the extreme-forward position, the flap has a smaller deflection that moves the centre of pressure forward relative to when the CG is in the extreme-aft position. A comparison of Figures 4, 6, and 8 illustrates the change in centre of pressure with respect to the flap angle for the three different operating conditions. To compensate for the negative lift produced at the trailing-edge by the increasingly negative flap deflections, higher angles of attack are required, as shown in Table 3. The hybrid airship mass at the low-speed operating condition is 1162 kg higher than at the two cruise-speed operating conditions. Table 6 shows that the increase in mass is due to the air contained within the ballonet at sea level compared to at cruise altitude where the ballonet is fully deflated. Figure 10 shows contours of streamwise skin friction and illustrates that some flow separation is observed at each operating condition (shown as regions where skin friction is negative). The lower-than-cruise-speed operating condition appears to have the largest area of separated flow regions. Tables 10 and 11 show surplus power of 18.4 kW at the lower-than-cruise-speed operating condition (cg-375) when flying at a constant velocity.

geometry	Full Span (m)	Root Chord (m)	Root Section Height (m)	Tip Chord (m)	Projected Area (m^2)	Surface Area (m^2)	Volume (m^3)
cg375	40.6	28.3	9.0	16.4	869.9	1938.0	3385.3
cg345	40.6	28.3	9.0	16.4	875.6	1931.1	3382.4
cg395	40.6	28.3	9.0	16.4	873.9	1923.5	3374.3

Table 4. Envelope geometry summary, 3-point-optimized full-solar hybrid airship

geometry	Envelope Mass (kg)	CtrlSurf Mass (kg)	Fuselage Mass (kg)	LandGear Mass (kg)	Payload Mass (kg)	Pilot Mass (kg)	Total Airship Mass (kg)
cg375	2909.5	473.3	936.3	245.2	500.0	84.0	5148.3
cg345	1743.5	471.6	936.3	245.2	500.0	84.0	3980.5
cg395	1738.0	469.8	936.3	245.2	500.0	84.0	3973.3

Table 5. Airship mass breakdown, 3-point-optimized full-solar hybrid airship

geometry	Env Surf Area (m^2)	Eff Sol Array Area (m^2)	Env Fab Mass (kg)	Env Gas Mass (kg)	Balnt Fab Mass (kg)	Balnt Gas Mass (kg)	Solar Array Mass (kg)	Total Env Mass (kg)
cg375	1814.9	570.3	618.5	527.4	144.0	1162.2	457.4	2909.5
cg345	1808.5	574.0	616.8	527.0	144.0	0.0	455.7	1743.5
cg395	1801.4	572.9	614.7	525.7	143.7	0.0	454.0	1738.0

Table 6. Envelope mass breakdown, 3-point-optimized full-solar airship

geometry	C_L	Aero Lift (kg)	Buoyant Lift Fraction	Buoyant Lift at Alt (kg)	Buoyant Lift at S.L. (kg)	OpEmpty Mass (kg)	Anchor Factor $\frac{\text{OEM}}{\text{B-lift-sl}}$
cg375	0.1988	1001.2	0.81	4147.0	4147.0	4564.3	1.10
cg345	0.1704	1062.0	0.73	2919.0	4143.5	4557.7	1.10
cg395	0.1710	1061.5	0.73	2912.0	4133.5	4547.7	1.10

Table 7. Airship lift breakdown, 3-point-optimized full-solar hybrid airship

geometry	C_D CFD	Drag CFD (N)	Friction Drag (N)	Pressure Drag (N)	Drag fuselage (N)	Drag env-x (N)	Drag total (N)	$\frac{L_{\text{aero}}}{D_{\text{total}}}$
cg375	0.0242	1157.6	312.4	845.2	613.4	503.4	2274.4	4.3
cg345	0.0181	1075.1	396.0	679.1	1073.6	624.8	2773.6	3.8
cg395	0.0181	1071.5	397.9	673.6	1073.6	623.6	2768.7	3.8

Table 8. Airship drag breakdown, 3-point-optimized full-solar hybrid airship

geometry	Aero Pitch Mmnt (Nm)	Buoy Pitch Mmnt (Nm)	Total Pitch Mmnt (Nm)	Center of Pressure (x/RC)	Center of Gravity (x/RC)	Neutral Point (x/RC)	Static Margin (%MAC)
cg375	169508.0	-169507.4	0.6	-0.24	0.38	0.49	0.12
cg345	143399.6	-143433.8	-34.2	-0.14	0.34	0.43	0.09
cg395	102030.2	-102027.8	2.4	0.05	0.39	0.44	0.05

Table 9. Airship trim and pitch stability, 3-point-optimized full-solar hybrid airship

geometry	Eff Solar Array Area (m^2)	Solar Power (kW)
cg375	570.3	74.1
cg345	574.0	74.6
cg395	572.9	74.5

Table 10. Airship power produced, 3-point-optimized full-solar hybrid airship

geometry	Motor Power (kW)	Aux Power (kW)	Total Power Consumed (kW)	Total Drag (N)	CtrlSurf Area (m^2)	Buoyant Volume (m^3)
cg375	31.0	24.6	55.7	2274.4	123.1	3385.3
cg345	50.1	24.6	74.6	2773.6	122.6	3382.4
cg395	50.0	24.5	74.5	2768.7	122.1	3374.3

Table 11. Airship power consumed, 3-point-optimized full-solar hybrid airship

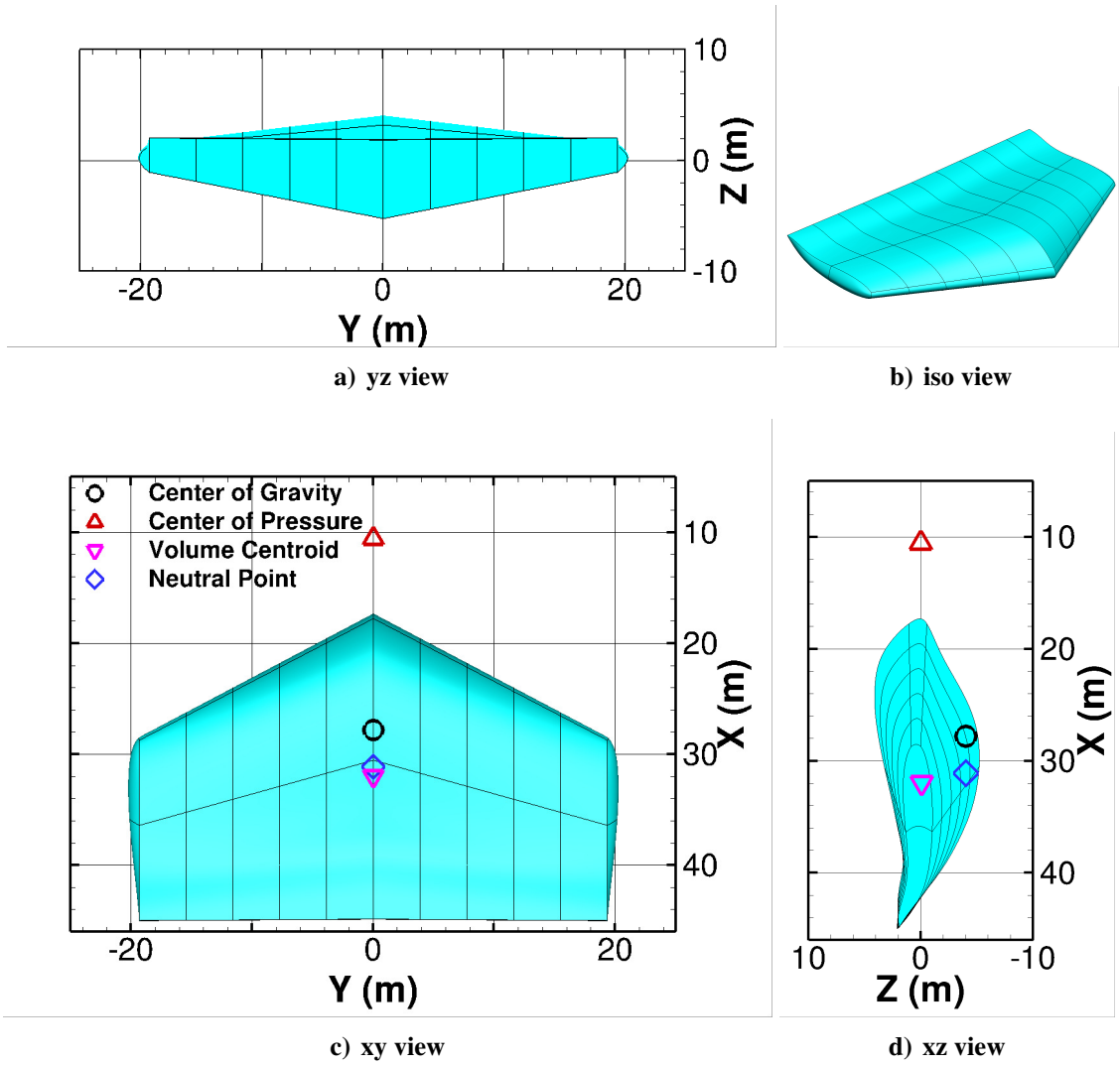

a) yz view **b) iso view**

c) xy view **d) xz view**

Figure 4. 3-point-optimized envelope geometry with prescribed CG at 37.5% x/RC. Cruise speed = 35 km/h, altitude = 0 m, Reynolds number = 18.62e6, AoA = 16.0°**, flap =** −28.1°

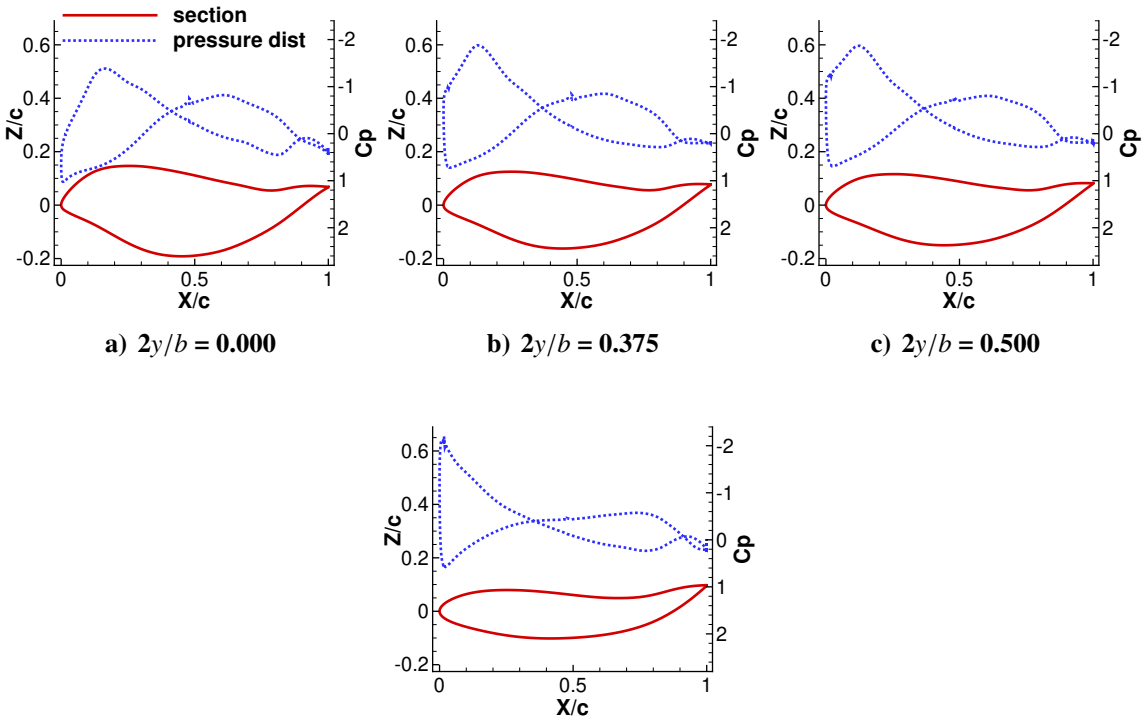

a) $2y/b$ **= 0.000** **b)** $2y/b$ **= 0.375** **c)** $2y/b$ **= 0.500**

d) $2y/b$ **= 0.875**

Figure 5. 3-point-optimized envelope geometry and spanwise pressure distributions. Trimmed, static margin of 12% MAC, CG at 37.5% x/RC, cruise speed = 35 km/h, Reynolds number = 18.62e6, AoA = $16.0°$**, flap =** $-28.1°$

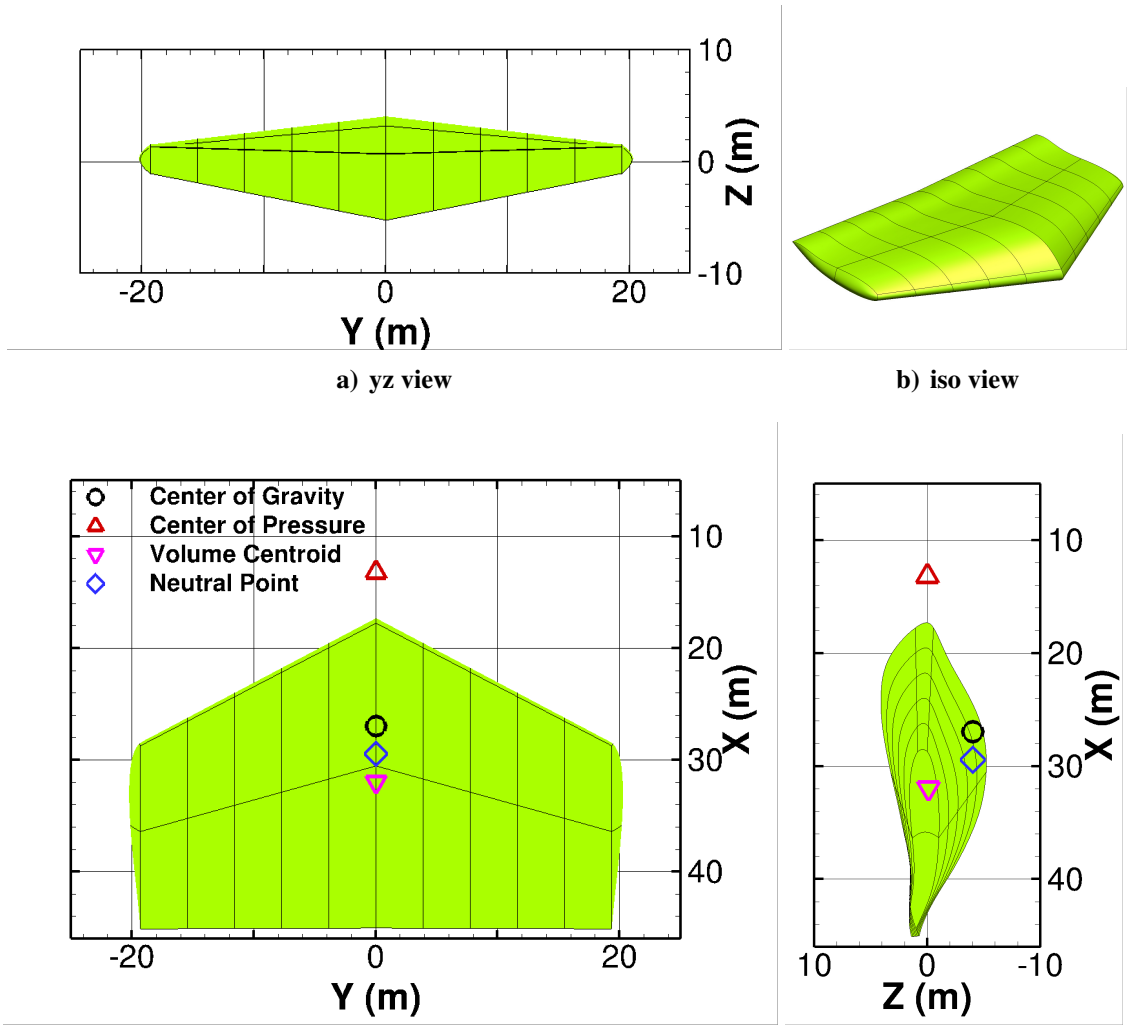

a) yz view

b) iso view

c) xy view

d) xz view

Figure 6. 3-point-optimized envelope geometry with prescribed CG at 34.5% x/RC. Cruise speed = 46.3 km/h, altitude = 3500 m, Reynolds number = 18.5e6, AoA = $11.2°$**, flap =** $-18.4°$

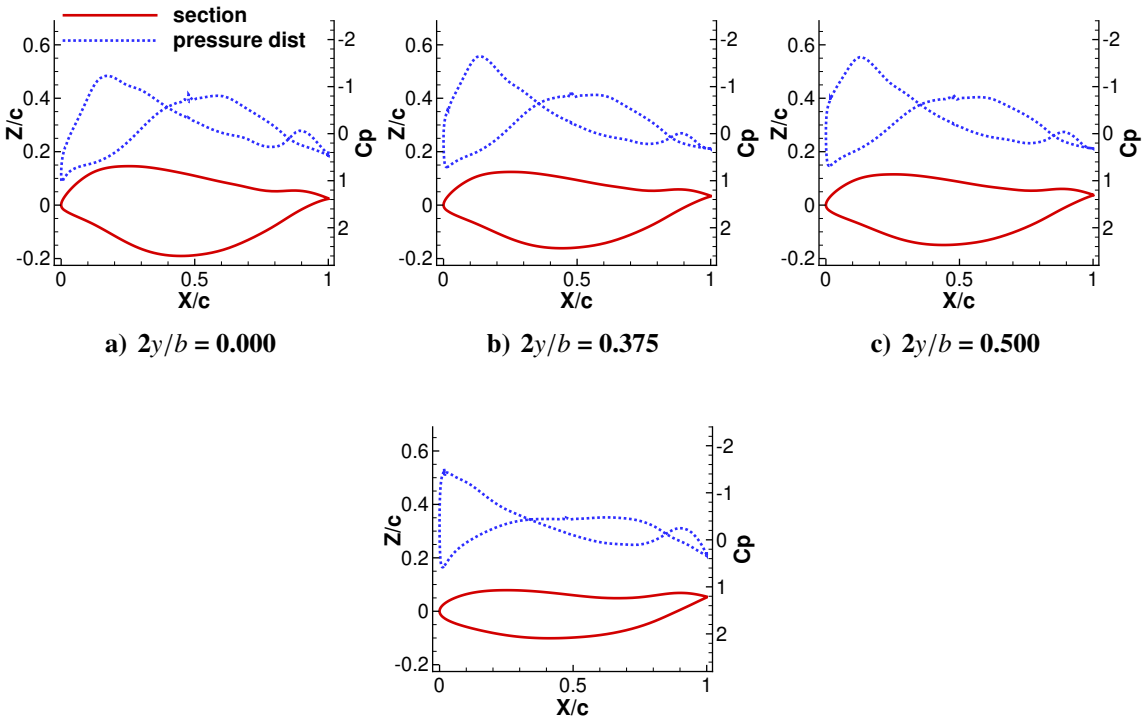

a) $2y/b$ **= 0.000** **b)** $2y/b$ **= 0.375** **c)** $2y/b$ **= 0.500**

d) $2y/b$ **= 0.875**

Figure 7. 3-point-optimized envelope geometry and spanwise pressure distributions. Trimmed, static margin of 9% MAC, CG at 34.5% x/RC, cruise speed = 46.3 km/h, Reynolds number = 18.5e6, AoA = $11.2°$**, flap =** $-18.4°$

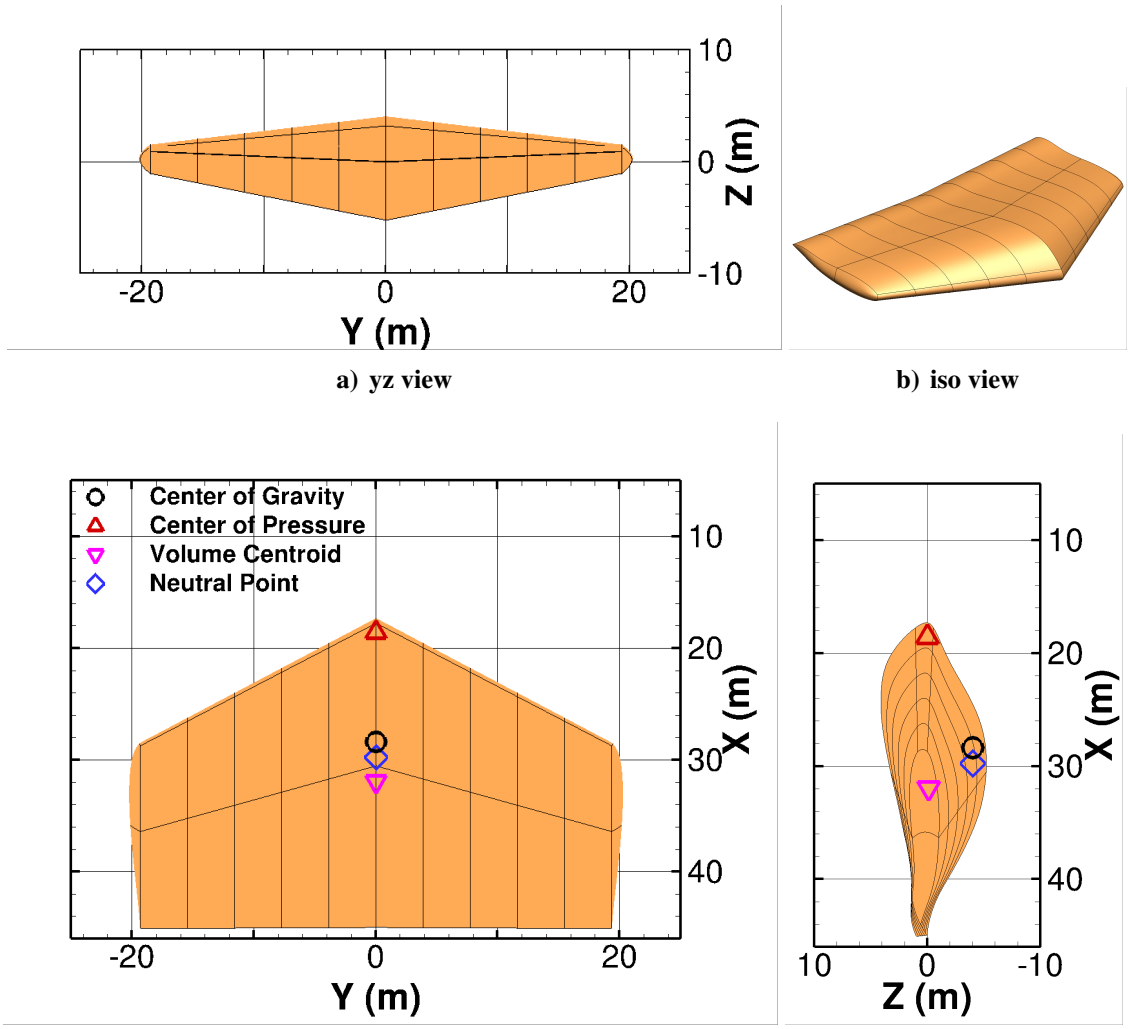

a) yz view

b) iso view

c) xy view

d) xz view

Figure 8. 3-point-optimized envelope geometry with prescribed CG at 39.5% x/RC. Cruise speed = 46.3 km/h, altitude = 3500 m, Reynolds number = 18.5e6, AoA = 7.9°, **flap =** 0.4°

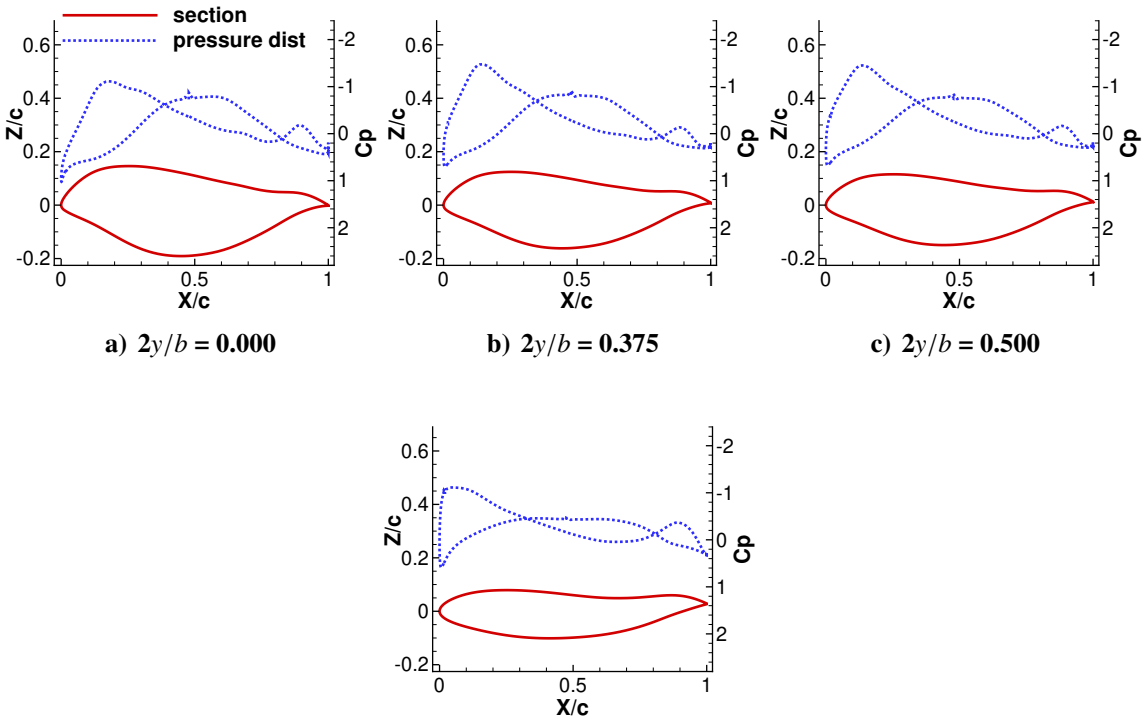

Figure 9. 3-point-optimized envelope geometry and spanwise pressure distributions. Trimmed, static margin of 5% MAC, CG at 39.5% x/RC, cruise speed = 46.3 km/h, Reynolds number = 18.5e6, AoA = $7.9°$**, flap =** $0.4°$

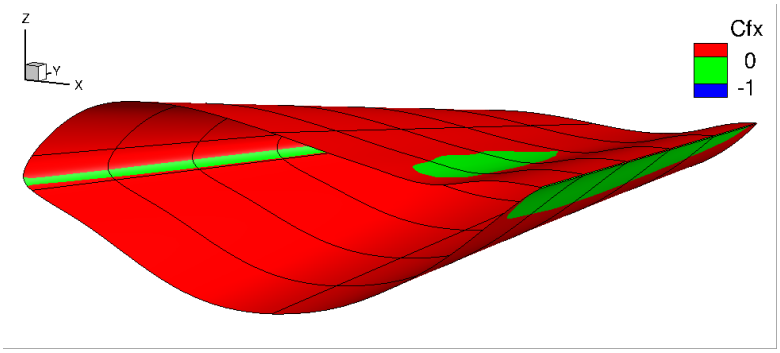

a) Speed = 35.0 km/h, Reynolds number = 18.5×10^6**, AoA =** $16.0°$**, flap =** $-28.1°$**, CG = 37.5% x/RC**

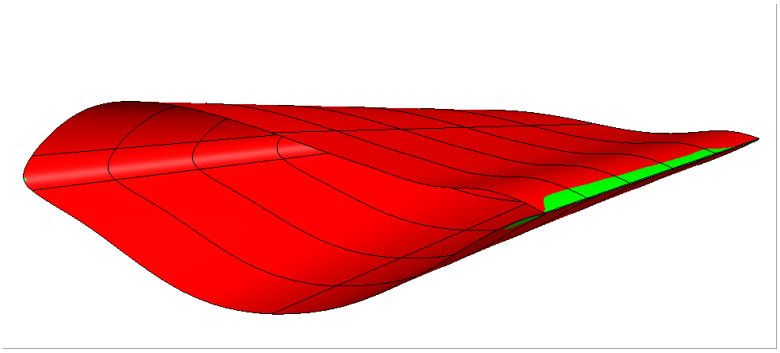

b) Speed = 46.3 km/h, Reynolds number = 18.6×10^6**, AoA =** $11.2°$**, flap =** $-18.4°$**, CG = 34.5% x/RC**

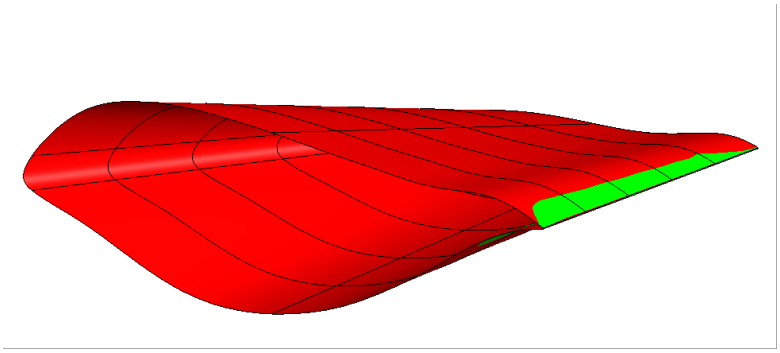

c) Speed = 46.3 km/h, Reynolds number = 18.6×10^6**, AoA =** $7.9°$**, flap =** $0.4°$**, CG = 39.5% x/RC**

Figure 10. Contours of streamwise skin friction showing regions of separated flow in green at each operating condition

geometry	AoA	β	Flap Angle	C_L	C_D	C_Y	C_l (roll)	C_m (pitch)	C_n (yaw)
cg375	16.0°	0.0°	−28.1°	0.1934	0.0223	0.000000	0.000000	0.1207	0.000000
cg345	11.2°	0.0°	−18.4°	0.1758	0.0177	0.000000	0.000000	0.0787	0.000000
cg395	7.9°	0.0°	0.4°	0.1745	0.0175	0.000000	0.000000	0.0560	0.000000
cg375	16.0°	0.5°	−28.1°	0.1933	0.0223	-0.000097	0.001111	0.1208	-0.000276
cg345	11.2°	0.5°	−18.4°	0.1758	0.0177	-0.000090	0.001053	0.0786	-0.000215
cg395	7.9°	0.5°	0.4°	0.1745	0.0175	-0.000110	0.001000	0.0560	-0.000208
cg375	16.0°	1.0°	−28.1°	0.1930	0.0223	-0.000206	0.002232	0.1208	-0.000554
cg345	11.2°	1.0°	−18.4°	0.1759	0.0177	-0.000180	0.002102	0.0786	-0.000430
cg395	7.9°	1.0°	0.4°	0.1746	0.0175	-0.000221	0.001998	0.0559	-0.000416

Table 12. Aerodynamic force and moment coefficients for the 3-point-optimized geometry evaluated on the full-span fine grid at side-slip angles of $\beta = 0.0°, 0.5°,$ and $1.0°$

C. Full-Span Fine-Grid Analysis of 3-Point-Optimized Geometry

The 3-point-optimized results described in Section V-B were achieved using a half-span geometry with coarse grid resolution sufficient for optimization cases. To analyze the performance of the optimized geometry when operating in a crosswind, a simulation of the airflow around the full-span geometry is required. A grid for the full-span envelope geometry with increased resolution has been created for this purpose. The optimal geometry is mirrored about the $X - Z$ symmetry plane at $y = 0$, and the number of grid nodes in each coordinate direction is increased by a factor of 1.5. Tables 12[b] and 13[c] show the aerodynamic force and moment coefficients and the roll, pitch, yaw moments for the 3-point-optimized geometry evaluated on the full-span fine grid described above at side-slip angles of $\beta = 0.0°, 0.5°$, and $1.0°$ respectively. The aerodynamic lift coefficients at cg375, cg345, and cg395 differ by -2.7%, +3.2%, and +2.0% respectively compared to the values of C_L for the optimized 3-point solution shown in Table 7 evaluated on the optimization grid. At a side-slip angle of $\beta = 1.0°$, the largest roll moment of 5.3 $kN \cdot m$ occurs at the cg345 operating condition and the largest yaw moment of 1.1 $kN \cdot m$ occurs at the cg375 operating condition. If we assume a linear relation between roll and yaw moments and side-slip angle, then a 10° cross wind would require ailerons that can counteract a 53 $kN \cdot m$ roll moment and rudders that can counteract an 11 $kN \cdot m$ yaw moment

During the optimization, a drag correction factor of 0.95 was applied to CFD drag values to

[b]A positive side-slip angle corresponds to a positive y-component of the hybrid airship velocity vector. Orientation of x,y,z axes corresponds to the right hand rule. The x-axis is parallel to the hybrid airship centerline

[c]Moments are positive corresponding to the right hand rule. Moments are calculated about the CG for each operating condition. See Figures 4, 6, and 8 for CG locations

geometry	β	Roll Moment $(kN \cdot m)$	Pitch Moment $(kN \cdot m)$	Yaw Moment $(kN \cdot m)$
cg375	0.0°	0.0	170.4	0.0
cg345	0.0°	0.0	137.6	0.0
cg395	0.0°	0.0	97.8	0.0
cg375	0.5°	2.3	170.4	-0.6
cg345	0.5°	2.7	137.6	-0.5
cg395	0.5°	2.5	97.8	-0.5
cg375	1.0°	4.6	170.6	-1.1
cg345	1.0°	5.3	137.4	-1.1
cg395	1.0°	5.1	97.7	-1.1

Table 13. Aerodynamic moments for the 3-point-optimized geometry evaluated on the full-span fine grid at side-slip angles of $\beta = 0.0°, 0.5°$, and $1.0°$

	Optimization	Medium	Fine	Continuum
Grid Size	2.3×10^6	15.1×10^6	35.3×10^6	∞
C_L	0.1951	0.1933	0.1886	0.1843
C_D	0.0242	0.0223	0.0214	0.0206
$\frac{C_L}{C_D}$	8.1	8.7	8.8	9.0
C_L Error	+5.8%	+4.8%	+2.3%	0.0%
C_D Error	+17.6%	+8.4%	+4.0%	0.0%
# of Blocks	64	128	128	-

Table 14. Grid convergence study for 3-point-optimized final envelope geometry. AoA = 16.0 degrees, Reynolds number 18.62×10^6, altitude = 0 m, vel = 35 kph. Calculated C_D order of accuracy is p = 1.8

account for expected error due to the coarse grid resolution used for optimization cases. A grid convergence study has been performed using the 3-point-optimized geometry to quantify the drag error for comparison with the drag correction factor. Results from the grid convergence study given in Table 14 show that for the low-speed case C_D is over-predicted by 17.6% on the optimization grid compared to the continuum value predicted by Richardson extrapolation. However, since the lift coefficient is decreasing with grid refinement, the continuum drag coefficient would be higher if calculated at the angle of attack needed to produce the required lift. Therefore the error in C_D is likely closer to 10%. In any case, the drag correction factor used in the optimization only reduces the drag by 5%, which implies that drag-related power calculations for the final design are conservative, thereby providing a margin of safety.

VI. Conclusions

An envelope has been designed for a solar-powered hybrid airship that is feasible at a cruise speed of 46 km/h. The envelope is small enough to fit through a hangar door of dimensions 48 m width

and 13 m height. The resulting design operates at high angles of attack and has some flow separation. This appears to arise as a result of the trim requirement at the low-speed operating condition. It is likely that a more efficient vehicle can be obtained if the centre of gravity can be shifted aft. Sensitivity studies indicate that smaller, faster hybrid airships will become possible with future improvements in solar panel irradiance. Future work is needed to ensure lateral stability and controllability, particularly for landing and take-off operations in a cross wind.

Acknowledgements

This research was made possible by funding from Solar Ship and the Government of Canada. Computations were performed on the GPC supercomputer at the SciNet HPC Consortium. SciNet is funded by: the Canada Foundation for Innovation under the auspices of Compute Canada; the Government of Ontario; Ontario Research Fund - Research Excellence; and the University of Toronto.

References

[1] Lutz, T. and Wagner, S., "Drag Reduction and Shape Optimization of Airship Bodies," *Journal of Aircraft*, Vol. 35, No. 3, 1998, pp. 345–351, doi:10.2514/2.2313.

[2] Haque, A. U., Asrar, W., Omar, A. A., Sulaeman, E., and Ali, J. M., "Conceptual Design of a Winged Hybrid Airship," *21st AIAA Lighter-Than-Air Systems Technology Conference*, June, 2014, pp. AIAA–2014–2710, doi:10.2514/6.2014-2710.

[3] Haque, A., Omar, A. A., Sulaeman, E., and Mohamed Ali, J. S., "Hybrid Buoyant Aircraft : Future STOL Aircraft for Interconnectivity of the Malaysian Islands," *Journal of Aviation Technology and Engineering*, Vol. 6, No. 2, 2017, doi:10.7771/2159-6670.1138.

[4] Hartmann, J., "Conceptual Design of Air Vehicles with Hybrid Lift Concepts - A Design Space Exploration," *55th AIAA Aerospace Sciences Meeting, AIAA SciTech Forum*, 2017, pp. AIAA–2017–1625, doi:10.2514/6.2017-1625.

[5] Zhang, L., Lv, M., Meng, J., and Du, H., "Optimization of solar-powered hybrid airship conceptual design," *Aerospace Science and Technology*, Vol. 65, June 2017, pp. 54–61, doi:10.1016/j.ast.2017.02.016.

[6] Hicken, J. E. and Zingg, D. W., "Aerodynamic Optimization Algorithm with Integrated Geometry Parameterization and Mesh Movement," *AIAA Journal*, Vol. 48, No. 2, 2010, pp. 400–413, doi:10.2514/1.44033.

[7] Osusky, L., Buckley, H., Reist, T., and Zingg, D. W., "Drag Minimization Based on the Navier-Stokes Equations Using a Newton-Krylov Approach," *AIAA Journal*, Vol. 53, No. 6, 2015, pp. 1555–1577, doi:10.2514/1.J053457.

[8] Reist, T. A., Zingg, D. W., Rakowitz, M., Potter, G., and Banerjee, S., "Multifidelity Optimization of Hybrid WingBody Aircraft with Stability and Control Requirements," *Journal of Aircraft*, Vol. 56, No. 2, 2019, pp. 442–456, doi:10.2514/1.C034703.

[9] Reist, T. A. and Zingg, D. W., "High-Fidelity Aerodynamic Shape Optimization of a Lifting-Fuselage Concept for Regional Aircraft," *Journal of Aircraft*, Vol. 54, No. 3, 2017, pp. 1085–1097, doi:10.2514/1.C033798.

[10] Gagnon, H. and Zingg, D. W., "Two-Level Free-Form and Axial Deformation for Exploratory Aerodynamic Shape Optimization," *AIAA Journal*, Vol. 53, No. 7, 2015, pp. 2015–2026, doi:10.2514/1.J053575.

[11] Gagnon, H. and Zingg, D. W., "Euler-Equation-Based Drag Minimization of Unconventional Aircraft Configurations," *Journal of Aircraft*, Vol. 53, No. 5, 2016, pp. 1361–1371, doi:10.2514/1.C033591.

[12] Koo, D. and Zingg, D. W., "Investigation into Aerodynamic Shape Optimization of Planar and Non-planar Wings," *AIAA Journal*, Vol. 56, No. 1, 2017, pp. 250–263, doi:10.2514/1.J055978.

[13] Lee, C., Koo, D., Telidetzki, K., Buckley, H., Gagnon, H., and Zingg, D. W., "Progress in Aerodynamic Shape Optimization Based on the Reynolds-Averaged Navier-Stokes Equations," *53rd AIAA Aerospace Sciences Meeting*, AIAA-2015-0262, Kissimmee FL, January 2015.

[14] Osusky, M. and Zingg, D. W., "A parallel Newton-Krylov-Shur flow solver for the Navier-Stokes equations discretized using summation-by-parts operators," *AIAA Journal*, Vol. 51, No. 12, 2013, pp. 2833–2851, doi:10.2514/1.J052487.

[15] Gill, P., Murray, W., and Saunders, M., "SNOPT: An SQP Algorithm for Large-Scale Constrained Optimization," *Society for Industrial Applied Mathematics Review*, Vol. 47, No. 1, 2005, pp. 99–131, doi:10.1137/S0036144504446096.

[16] Jameson, A., "Aerodynamic Design Via Control Theory," *Journal of Scientific Computing*, Vol. 3, No. 3, June 1988, pp. 233–260, doi:10.1007/BF01061285.

[17] Osusky, M., Boom, P. D., and Zingg, D. W., "Results from the Fifth AIAA Drag Prediction Workshop obtained with a parallel Newton-Krylov-Schur flow solver discretized using summation-by-parts operators," *31st AIAA Applied Aerodynamics Conference*, 2013, pp. 1–20, doi:10.2514/6.2013-2511.

[18] Chernukhin, O. and Zingg, D. W., "Multimodality and Global Optimization in Aerodynamic Design," *AIAA Journal*, Vol. 51, No. 6, 2013, pp. 1342–1354, doi:10.2514/1.J051835.

[19] Nocedal, J. and Wright, S. J., *Numerical Optimization, Second Edition*, Springer, 2006, pp. 320–321, doi:10.1007/978-0-387-40065-5.